6-DoF Motion Capture with Nanometric Resolutions over Millimetric Ranges Using a Pseudo-Periodic Encoded Pattern

Belal Ahmad, Patrick Sandoz, Guillaume J. Laurent

Abstract—We propose a method to measure the six degrees of freedom (DoFs) of an object moving in space with nanometric resolutions over millimetric ranges. Similar to conventional motion capture systems, a marker is attached to the object and tracked using an imaging system. However, the proposed method relies on digital holography rather than conventional refractive microscopy and involves two complementary measurement principles, i.e., interferometry and phase-based motion estimation, applied simultaneously to the hologram of a micro-structured pattern. Interferometry addresses out-of-plane motions, while phase-based motion estimation addresses complementary in-plane displacements to address the six DoFs. Performance metrics, namely, resolution, linearity, range, and repeatability, are evaluated experimentally. Finally, the proposed measurement method is applied to capture the motion of a precision hexapod to demonstrate its potential for 3D metrology applications at the nanometer scale.

Index Terms—Motion capture, fiducial markers, digital holography, precision robotics, nanopositioning

I. Introduction

The remote measurement of the six degrees of freedom (DoFs) of moving objects has advanced drastically in recent decades. Motion capture systems have become indispensable to filmmaking, video game development, and indoor mobile robotics. In industry, laser trackers are the tool of choice for the metrology and calibration of robotic manipulators. In outdoor spaces, the global navigation satellite system is essential for locating phones, vehicles, and drones. However, at a microscopic scale, there is a high demand for such versatile measurement systems that could track the six DoFs of an object with nanometric resolutions over relatively large ranges.

At a macroscopic scale, various 6-DoF versatile measurement systems, including laser trackers and motion capture systems, exist. Motion capture systems use several sensors, typically cameras and inertial measurement units, to track the motion of different parts of the target object. This allows the estimation of the six DoFs of an object in 3D space with sub-millimetric resolution. Recent motion capture systems can

provide a range of 15 m with a resolution of 0.1 mm. In addition to filmmaking and video games, they are used for indoor robotics [1], industrial metrology [2], animal studies [3], and even biomedical applications [4]. On the other hand, industrial laser trackers consist of laser interferometers and goniometers to provide 6-DoF measurements using multiple reflective targets on the measured object. They can reach a range of 80 m with a resolution of 0.5 µm for distance measurements along the laser axis [5], [6], [7].

At the microscopic scale, position sensors such as capacitive [8], piezoresistive [9], inductive [10], and optical [11] ones are well-known and widely used. These sensors can offer a range in the order of hundreds of micrometers, with a resolution down to hundreds of picometers for the most precise of them [12]. Moreover, interferometers provide a very high range-to-resolution ratio of approximately 10^9 along the laser's axis. Considering that these techniques can mostly provide measurements for only one DoF (one sensor is used for each motion axis), the design of small-scale motion-sensing applications is challenging. For instance, some combinations of interferometers enable multiple DoF measurement systems [13], [14], at the expense of occupied volume and costs. These systems can provide up to six DoF measurements with nanometric and subnanometric resolutions using techniques such as grating-based interferometry [15] and surface encoders [16]. However, due to the constraints of the laser reflections, the ranges of the angle measurements are very low, in the order of magnitude of one milli-radian.

An alternative way for multi-DoF measurements at the microscale can be realized by phase-based motion estimation using optical microscopes and microfabricated encoded patterns, which can reach up to three DoFs with a high range-to-resolution ratio of 10^8 in the plane [17], [18], [19]. Vision-based measurements are widely used in micro-robotics. It is simple to set up because only a microscope, camera, and microfabricated pattern are required to track the target's motion [20]. However, due to the nature of conventional microscopy, vision-based measurements are limited to in-plane motion, whereas out-of-plane measurements require scanning multiple out-of-plane positions of the target. Confocal microscopy offers an appealing technology to obtain out-of-plane measurements by scanning the target with a focused light using galvano mirror scanners and stages. It offers nanometric resolution by using a pinhole to focus on a specific depth of the target, eliminating out-of-focus blur [21]. For example, Tan et al. proposed a laser confocal feedback tomography system that

can provide distance measurements with a resolution of 2 nm over an unambiguous range of 10 μm [22]. Nonetheless, the need to scan the target limits the applications of confocal microscopy in motion capture, where multi-DoF measurements are required in one shot. The same scanning requirement limit was observed in an early attempt to access six DoFs using interferometry [23].

In this study, we propose a motion capture system dedicated to small-scale measurements based on off-axis digital holography. Digital holographic microscopes (DHM) use interferometry to provide depth measurements by digitally processing the interferometric fringes formed on a camera (called holograms). The off-axis DHM introduces a fringe carrier in which frequency and phase are modulated according to the target's elevation. In addition, DHM extends the depth-of-focus of microscope lenses by one order of magnitude or more. Consequently, it can provide sample topography with a nanometric resolution over a range of hundreds of micrometers. This makes the DHM highly suited for topography measurements in a single shot without lateral or vertical scans [24], [25].

To use a DHM as a motion capture device, the six DoFs of an object of interest must be estimated from a single holographic image. Two main issues need to be addressed: the in-plane and out-of-plane pose estimation. To measure the three out-of-plane DoFs, we propose a method that uses the off-axis fringes and reconstructs a regression plane of a planar target directly from the spectral representation of the hologram. This method estimates the elevation z and the out-of-plane angles β and γ of the target with nanometric and sub-microradian resolutions, respectively. The remaining three DoFs are the two translations x and y, and the rotation around the optical axis α. To capture these DoFs, we propose to use of a specific pseudo-periodic pattern engraved in the target, which provides absolute and redundant position information. The calculation of the spatial phase of this pattern in the frequency domain has demonstrated the absolute position estimation of the three in-plane components with nanometric resolution over centimeters ranges in the case of conventional refractive microscopy [18]. However, the previously developed method cannot be applied to holographic images without the specific pre-processing proposed in this article.

The integration of these two methods results in the estimation of the six DoFs of the pattern from a single holographic image. Fig. 1 provides a conceptual illustration of the proposed measurement system. The proposed technique allows full pose estimation with nanometric resolutions over millimetric ranges with a single device and a single shot. This measurement system can have a major impact on several industrial tasks, such as photolithography [26], micro-assembly [27], metrology [28], [29], and micro-force measurements [30], [31]. For example, optical fiber alignment requires the estimation of the fibers' relative poses in 3D, i.e., at least five DoFs including three position components and two orientation components, with nanometric precision to achieve a high optical coupling efficiency [32].

In the following, section II presents the method measurement principle. Then experiments and results are presented in
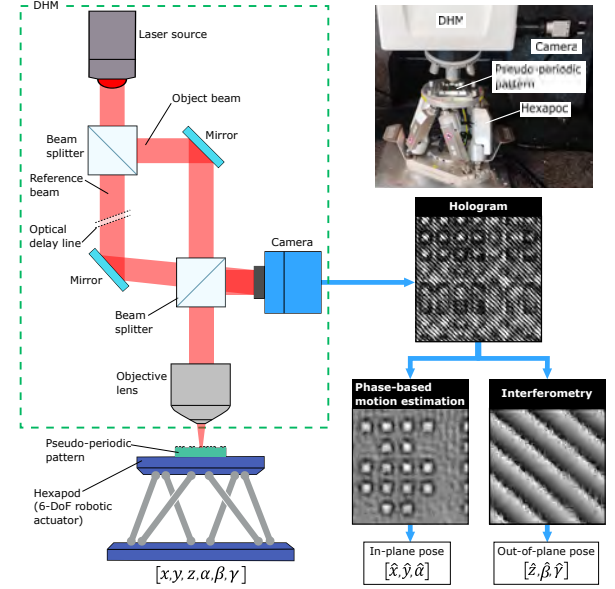

Figure 1. Concept of the proposed 6-DoF measurement system. *(Left)* An illustration showing the components of the measurement system, including the different components of the DHM, pseudo-periodic encoded pattern, and 6-DoF hexapod. *(Top-right)* A picture of the measurement system showing its different components. *(Bottom-right)* A simplified block diagram showing an overview of the hologram processing to estimate the 6-DoF pose of the robot.

section III, with a first part dedicated to demonstrate ultimate method performances and a second part reporting on the method application to a precision hexapod. Finally, section V concludes the paper.

II. Position Measurement Principle

The developed method involves two complementary measurement principles, i.e., interferometry and phase-based motion estimation. These principles are applied simultaneously to a pseudo-periodic encoded pattern that constitutes a known reference object from which motions are retrieved. Interferometry addresses out-of-plane motions, whereas phase-based motion estimation addresses complementary in-plane displacements to tackle the six DoFs. Moreover, these two principles share phase computations as a powerful means to achieve high resolutions. The pattern has been designed to optimize the performance of both interferometry and phase-based motion estimation principles. We apply interferometry in an original way, based on the *a priori* knowledge of the observed pattern, as described in section II-A. The phase-based approach used for in-plane measurements has already been demonstrated in the case of conventional imaging with no or low sensitivity to out-of-plane motion [18], [33], [34]. Therefore, its principle is described more succinctly in section II-B.

A. Out-of-plane measurements

Interferometry is based on the wave character of light and converts optical paths into cosine-shaped fringe signals. The strength of interferometry relies on its high sensitivity because the transition between two consecutive signal extrema

requires a displacement of only half a wavelength. However, interferometry presents three types of ambiguities: *i)* At the horizontal tangent positions of the cosine function, discrimination between forward and backward displacements is lost. *ii)* The cosine function has the same response for positive and negative arguments, which introduces a sign ambiguity on the measured optical paths. *iii)* The periodic character of the cosine function induces an ambiguity of an entire number of periods.

One way to overcome the first two limitations is to practice phase shifting, either in parallel or sequentially. Another way consists of introducing a high-frequency fringe carrier to avoid problematic cases, *i.e.*, sign uncertainty, and forward/backward transitions. The advantage of the second option is that it complies with single-shot recording, thus facilitating real-time measurements. Various options are also proposed to overcome the third ambiguity of an entire number of periods. The simplest one is to use a sufficiently high sampling rate to ensure that consecutive samples are separated by less than half a wavelength, thereby allowing secure phase unwrapping. The other option consists of using two or more wavelengths in parallel to solve the ambiguity through the relative phase shifts associated with the different wavelengths [35].

These multiple options have led to many interferometric measurement devices suited to a wide array of applications. In this study, we used off-axis DHM that applies the high-frequency fringe carrier technique to avoid the first two ambiguity sources. We conducted our experiments in reflection mode with a single wavelength. We thus hypothesized that consecutive out-of-plane positions are distant by less than a quarter of a wavelength in z. However, the DHM method and device used work exactly in the same way with two or three wavelengths. We chose to discard this possibility for the sake of simplicity in explaining and understanding the 6-DoF measurement principles involved.

A major advantage of DHM is that it extends the allowed working range of microscope lenses. Indeed, DHM deliberately does not record in-focus images but blurred defocused ones. The effect of diffraction is then compensated numerically through back-propagation computations suited to reconstructing in-focus images digitally. Back-propagation computations are made possible by the interferometric character of DHM, which gives access to both the amplitude and phase of the light waves involved. Owing to this numerical trick, the working ranges of microscope lenses are extended by one order of magnitude or even more [36], [37].

The principle of off-axis DHM is shown in Fig. 1, with the setup scheme on the left-hand side and views of the actual device used and a zoom of a recorded hologram, allowing further 6-DoF retrieval on the right-hand side. The light beam issued from the laser source is separated to feed the two interferometer arms. The object beam is directed at the camera after reflection on the micro-structured pattern fixed onto the robot of interest. The reference beam is also directed toward the camera but with an incident angle to produce the expected fringe carrier frequency. The lengths of the two interferometer arms are adjusted through a delay line to differ by less than the coherence length of the light source to produce interferences

on the camera. Because of diffraction, the recorded holograms provide blurred views of the pattern superimposed on a regular set of interference fringes as observed in the hologram zoom.

From a mathematical perspective, the two light waves incident on the camera sensor are defined as:

$$\mathcal{A}_{ref}(m,n,t) = a_{ref}(m,n) \cdot e^{iwt} \cdot e^{i\Phi_{ref}(m,n)} \quad (1)$$

and

$$\mathcal{A}_{obj}(m,n,t) = a_{obj}(m,n) \cdot e^{iwt} \cdot e^{i\Phi_{obj}(m,n)} \quad (2)$$

where w is the light pulsation equal to $\frac{2\pi}{\lambda}$ with λ the light wavelength. $a_{ref}(m,n)$ and $a_{obj}(m,n)$ are the local amplitudes of the reference and object waves, respectively. m and n are the pixel coordinates. The local phases $\Phi_{ref}(m,n)$ and $\Phi_{obj}(m,n)$ are defined by:

$$\Phi_{ref}(m,n) = \Phi^0_{ref} - (m - m_c) \cdot p \cdot \sin(\beta_{ref}) + (n - n_c) \cdot p \cdot \sin(\gamma_{ref})\cos(\beta_{ref}) \quad (3)$$

$$\Phi_{obj}(m,n) = \frac{4\pi}{\lambda}z - (m - m_c)\frac{p}{M}\sin(\beta_{obj}) + (n - n_c)\frac{p}{M}\sin(\gamma_{obj})\cos(\beta_{obj}) \quad (4)$$

where (m_c, n_c) are the pixel coordinates of the optical axis, p the pitch of the image sensor, γ_{ref} and β_{ref} are the inclinations of the reference wave with respect to the x and y sensor axes, respectively. Φ^0_{ref} is a constant phase term in the interval $]-\pi., \pi]$. M is the imaging lens magnification, γ_{obj} and β_{obj} are the observed pattern inclinations and z is the elevation of the observed pattern at its intersection at the optical axis. Eq. 4 assumes the observed object is plane, for instance a mirror, fully defined by its out-of-plane orientation and its elevation at its intersection with the optical axis.

Because of the interference phenomenon, the hologram intensity is made of a DC background modulated by fringes corresponding to the cosine of the hologram phase, which is determined by the difference between the reference and object phases as follows:

$$\Phi_{hol}(m,n) = \Phi_{ref}(m,n) - \Phi_{obj}(m,n) \quad (5)$$

At the hologram center, we obtain:

$$\Phi_{hol}(m_c, n_c) = \Phi^0_{ref} - \frac{4\pi}{\lambda}z \quad (6)$$

This equation shows that the hologram phase at the imaging center of the camera provides a direct measure of the observed pattern elevation z modulo $\lambda/2$.

$$z = \frac{\lambda}{4\pi}\left(\Phi^0_{ref} - \Phi_{hol}(m_c, n_c)\right) \quad (7)$$

If we derive the hologram phase with respect to the two image sensor directions, respectively, we obtain a direct measure of the out-of-plane angles γ_{obj} and β_{obj} of the object through the modulation of the fringe carrier phase slope:

$$\frac{\partial \Phi_{hol}}{\partial m} = -p \cdot \sin(\beta_{ref}) + \frac{p}{M}\sin(\beta_{obj}) \quad (8)$$

and

$$\frac{\partial \Phi_{hol}}{\partial n} = p \cdot \sin(\gamma_{ref})\cos(\beta_{ref}) - \frac{p}{M}\sin(\gamma_{obj})\cos(\beta_{obj}) \quad (9)$$

In practice, the frequency carrier is isolated in the Fourier spectrum of the hologram using a Gaussian band-pass filter. After the inverse Fourier transform of the filtered spectrum, we directly obtain the wrapped phase associated with the frequency carrier. The phase derivatives and their values at the optical axis intersection are retrieved after phase unwrapping and the least square fitting of the plane phase map. This procedure is depicted in supplementary videos. In video 1, the fringe carrier is identified as a sharp peak in the hologram Fourier spectrum, and a narrow band-pass filter is centered on this peak. After inverse Fourier transformation, we directly obtain the wrapped phase associated with the carrier frequency, and, after phase unwrapping, the least mean square coefficients of the best fitting plane give the fringe carrier frequency from which the pattern orientation is deduced. In video 1, we can observe the large displacement of the spectral peak associated with the fringe carrier for both β and γ angles in a range of $(-0.11, 0.11)$ rad. Intermediary phase maps also show the phase distributions obtained without and with subtraction of the mean carrier frequency. The tip and tilt measurements retrieved in this way are thus relative to the incident angle attributed to the reference beam and are not related to any actual world horizontal reference.

Supplementary video 2 focuses on the extraction of the elevation z and the compensation of 2π phase jumps. When the pattern is moved along the axial z direction, it is the phase of the carrier frequency that is changed rather than its frequency. However, the same phase computations allow the accurate determination of these variations, provided that the z-displacement between consecutive holograms remains smaller than the ambiguity range of $\lambda/4$ (in reflection mode, the round-trip beam travel sets the ambiguity range to one-quarter of a wavelength). In video 2, the phase variations associated with the sliding of the frequency carrier can be observed. Their determination leads to accurate z measurements.

This unusual way of processing DHM holograms applies to our 6-DoF motion capture application because we know that the observed sample is flat and can thus be assimilated to a plane surface. In practice, our pattern is not perfectly flat because of its microstructure. However, regarding the size of the observed area, the small height ($110\,\mathrm{nm}$) and regular distribution of the dots induce sufficiently small alterations of the average flatness to keep the resulting errors smaller than the method's resolution. To verify this assumption, we repeated the same experiments with a mirror and with our micro-structured pattern, and we got the same level of performance: the effect of the pattern micro-structure is drowned in the detection noise.

One may notice that these out-of-plane measurements are performed along the optical axis of the DHM device and are not attached to a particular point of the object. For instance, a lateral displacement of a tilted pattern leads to apparent z variations. The latter results from the observation of neighbor points on the oblique pattern, even if the pattern moves horizontally. This effect has to be addressed properly in reconstructing actual 3D trajectories.

B. In-plane position measurements

Phase-based correlation has been successfully applied to in-plane motion detection in different ways. The use of the object's natural texture as a detection pattern is the most general and direct way. In this case, however, performances are object-dependent, and resolution is limited to approximately $1/10^{th}$ of a pixel. Improved performances are obtained using a structured pattern specifically designed to optimize image processing accuracy. At the micro-scale, the fabrication of such dedicated patterns is much more acceptable than at the macro-scale because the sizes involved remain small. Furthermore, micro-electronics clean room processes are readily available to realize highly accurate masks. The latter constitute size references embedded in the target of interest and available in every image recorded. Therefore, such approaches are self-calibrating as long as the pattern size is reliable. In our case, we conceived a pseudo-periodic pattern allowing the absolute encoding of a large area as well as robust position decoding of the current view observed. Our approach combines relative but fine measurements, relying on the periodic character of our pattern, with coarse but absolute measurements based on the binary code encrypted through the missing dots, altering the pattern's periodicity. Full details can be found elsewhere [18], [33]. Our pattern design presents the advantages of preserving the phase linearity and allowing extended in-plane ranges. It appears to be the best solution in terms of range-to-resolution ratio [17].

In our application based on digital holography, the in-focus image of the pattern is not directly recorded by the camera but has to be reconstructed numerically from the hologram. The well-known procedure consists of back-propagating the light wave to the right distance to obtain the in-focus image [38]. The most popular method used for this purpose is based on the angular spectrum method, which is also used by our DHM device [39]. The most difficult task consists of determining the correct distance to obtain the best in-focus image after numerical back-propagation of the hologram. This step can be performed empirically or using auto-focus algorithms [40]. In the 3D motion capture application, this task has to be performed only once because the measured z-displacements allow the continuous update of this critical parameter. In practice, the best z reconstruction distance is determined empirically before object motion and then continuously updated with measured z displacements. The depth-of-focus of the $10\times$ microscope lens used is approximately $10\,\mu\mathrm{m}$, and this value corresponds to the acceptable tolerance in the initial z-distance determination and this value is comfortable.

The object reconstruction principle is illustrated in Fig. 2. The Fourier spectrum of the hologram is filtered to keep only the first-order lobe. The latter is then propagated numerically to the chosen reconstruction distance by applying the suited phase term to every spectral component [39]. Finally, an inverse Fourier transform is applied to the propagated Fourier spectrum to obtain the reconstructed object in both phase and intensity. This pattern reconstruction principle is illustrated in supplementary video 3 that reproduces Fig. 2 for a z-scanning sequence. We can observe the phase variations associated with
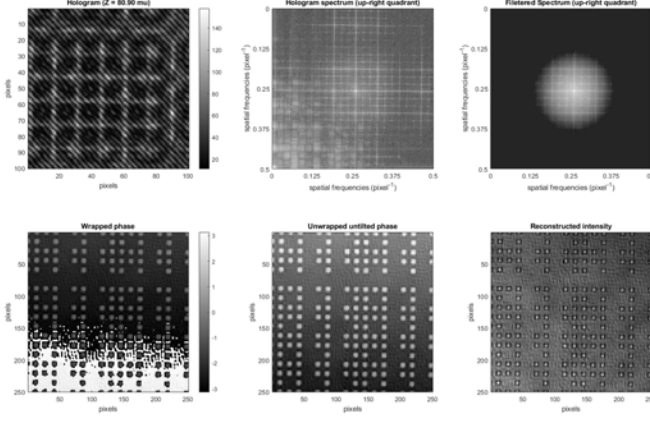
Figure 2. Pattern reconstruction from the recorded hologram. *(Top-left)* Small zone of the recorded hologram. *(Top-center)* Upper-right quadrant of the Fourier spectrum of the hologram. *(Top-right)* Filtered spectrum before angular spectrum propagation and inverse Fourier transform. *(Bottom-left)* Reconstructed wrapped phase map. *(Bottom-center)* Phase map after phase unwrapping and least square mean plane subtraction. *(Bottom-right)* Reconstructed pattern intensity.
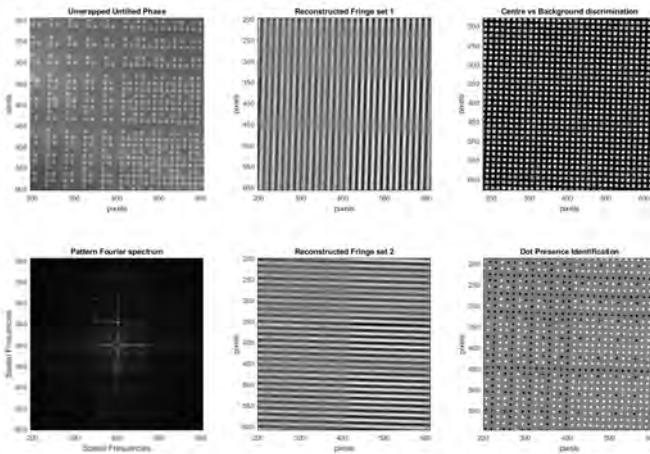

Figure 3. In-plane position measurement from reconstructed pattern data. *(Top-left)* Unwrapped untilted phase map obtained from hologram reconstruction. *(Bottom-left)* Fourier spectrum of the phase map with circles on the main direction spatial frequencies. *(Middle)* Reconstructed fringe sets after inverse Fourier transform of the spectrum filtered around the magenta (top) and red (bottom) circles, respectively. *(Top-right)* Dot location derived from the phase data. *(Bottom-right)* Identification of dot presence or absence from local thresholding for further binary position decoding.

the elevation of the object and the flow of noise.

Once the pattern image is reconstructed, phase analysis can be either applied to the intensity map or the phase map after unwrapping and mean tilt removal (cf. Fig. 2). Its purpose is to retrieve which position of the encoded pattern is imaged exactly at the center of the recorded hologram. Once again, phase computations are involved, and image processing starts with a Fourier transform. It allows the demultiplexing of the two main directions of the pattern that lead to well-separated spectral lobes (Fig. 3(bottom-left)). After Gaussian filtering, the inverse Fourier transform of lobes f_1 (resp. f_2) leads to 1D fringe sets, as represented in the middle of the figure and for the magenta (top) and red (bottom) spectral peaks, respectively. The wrapped phase associated with these 1D

fringe sets is also provided by the inverse Fourier transform and is used for the next steps of position retrieval. On the one hand, after phase unwrapping, the least squares fitting of those phase maps is representative of the subpixel positioning of the pattern with respect to the pixel frame of the recorded image. On the other hand, the location of the pattern of white dots is detected as the position where the phase is close to zero for both fringe sets. Conversely, positions where one wrapped phase is close to $\pm\pi$ correspond to the pattern background; i.e. inter-dot pixels. This phase-based discrimination is represented on the top-right part of the figure and allows the definition of a local threshold suited to determining whether corresponding dots are present or absent (bottom-right part of the figure). This phase-based processing leads to a robust determination of the in-plane position of the tiny zone observed in this view within the whole pattern [33]. Nominal performances for in-plane position measurement are summarized in Table I, where nanometric resolution in lateral positioning and a few micro-radian resolutions in orientation are achieved [18]. Full method details and performances can be found elsewhere [18], [33].

III. EXPERIMENTS AND RESULTS

In the following sections, the experimental system will be explained and the performance metrics, namely, resolution, linearity, range, and repeatability, of the proposed method will be demonstrated. In this study, two types of experiments were conducted: i) characterization experiments and ii) application experiments. The characterization experiments focused on the out-of-plane components of the robot pose, as the in-plane metrics are the same as those obtained with conventional microscopes. For this, a high-precision piezoelectric nanopositioning stage (P-528.TCD, Physik Instrumente GmbH & Co. KG.) capable of 3-DoF out-of-plane motion was used as a reference positioning system. In the application experiments, the performance of the proposed method for 6-DoF motion capture was demonstrated by estimating the full pose of a precision hexapod (HXP50-MECA, Newport Co.) in different scenarios.

A. Experimental system and data acquisition and analysis

The experimental system used for the characterization of the proposed method consists of a DHM (R2100, Lyncee Tec SA, Switzerland). The DHM is equipped with a laser having a wavelength of 675 nm and can record holographic images at a frame rate of 150 fps using a CMOS camera (Basler acA1920-155um). A $10\times$ objective lens (Leica 506505, N.A. 0.3) is mounted on the DHM to focus the laser beam on the measured sample. The DHM is mounted on a manual z-stage to adjust its vertical position. A piezoelectric stage (P-528.TCD, Physik Instrumente) that can generate out-of-plane displacements (z, β, γ) is fixed under the DHM. The stage has a range of 200 µm, 2 mrad, and 2 mrad, a resolution of 1 nm, 0.1 µrad, and 0.1 µrad, and a linearity error of 0.03%, 0.15%, and 0.15% on z, β, and γ, respectively. Both the DHM and the piezo stage are mounted on a granite block, and the entire structure is enclosed inside a homemade plastic box, which helps in reducing airflow and stabilizing the temperature of the
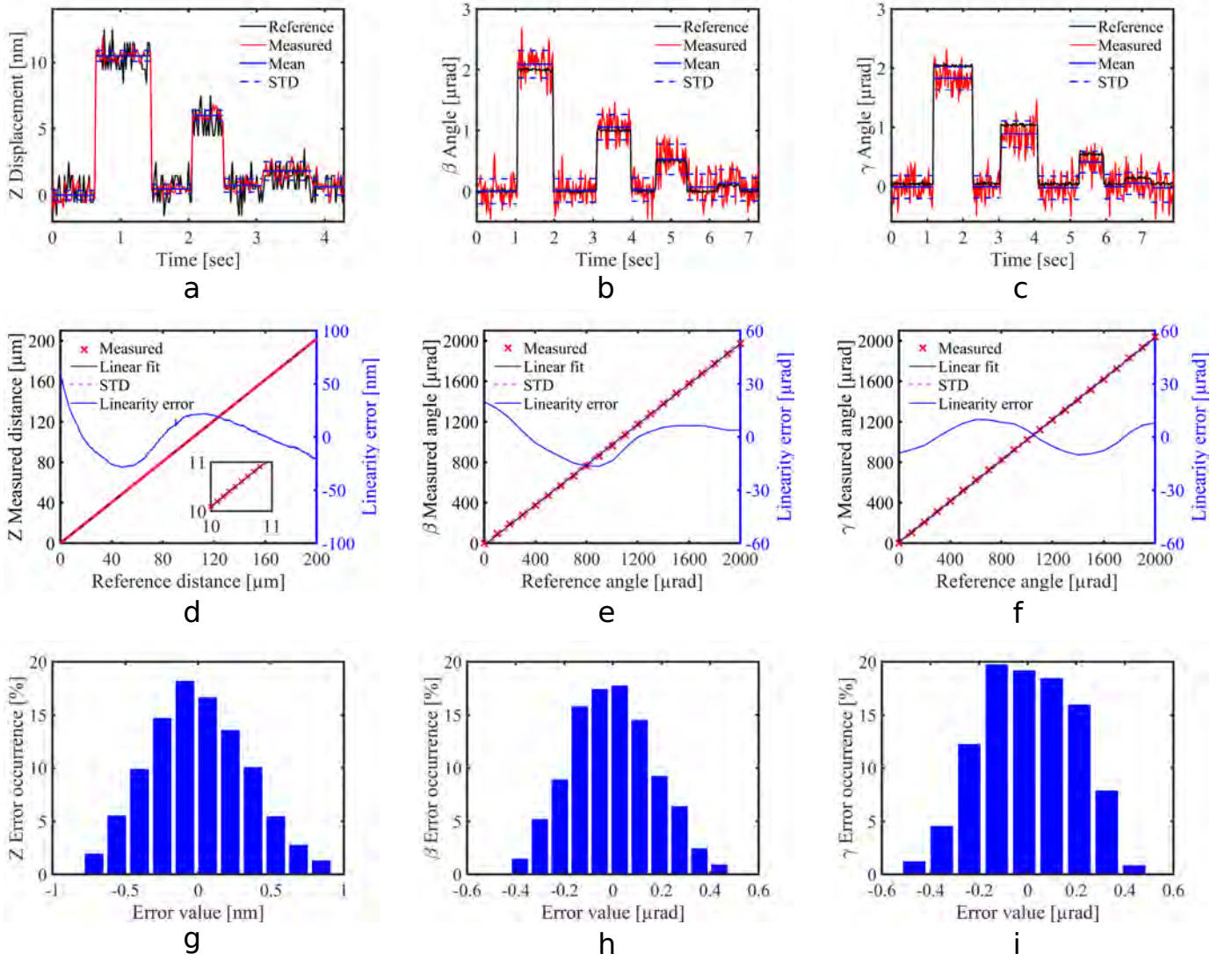
Figure 4. Characterization of out-of-plane measurements using a 3-DoF nanopositioning piezoelectric stage. (a-c) Resolution tests using square waves with descending amplitudes for each out-of-plane axis, z, β, and γ, respectively. The black lines, red lines, blue-solid lines, and blue-dashed lines represent the reference position acquired from the stage sensors, the measured position by the proposed method, the mean measured position using the proposed method, and the standard deviation using the proposed method, respectively. (d-f) Linearity tests for each each out-of-plane axis, z, β, and γ, respectively. The inset in (d) shows a zoom-in view. The red crosses, black lines, magenta-dashed lines, and blue lines represent the measured position by the proposed method, the linear fit of the measured points, the standard deviation of the linear fit, and the linearity error, respectively. (g-i) Repeatability tests for each out-of-plane axis, z, β, and γ, respectively. The figures show the histogram of the repeatability errors for each axis.

environment surrounding the experimental system. Finally, the total system is mounted on an anti-vibration table (Newport Vision IsoStation) to reduce vibration disturbances.

The top right image in Fig. 1 shows the experimental system that is used for the 6-DoF robotic application. The system is similar to the previous system. However, a hexapod (HXP50-MECA, Newport Co.) that can generate in-plane and out-of-plane displacements (x, y, z, α, β, γ) was fixed under the microscope, replacing the piezo stage. The hexapod has a range of ±17 mm, ±15 mm, ±7 mm, $\pm9°$, $\pm 8.5°$, and $\pm18°$ and a resolution of 100 nm, 50 nm, 50 nm, 50 µdeg, 50µdeg, and 100 µdeg corresponding to x, y, z, α, β, γ, respectively.

The DHM, piezo stage, and hexapod are connected to a main PC for high-level control and data acquisition. A C# program is used to control the different components

of the system and to synchronize the data acquisition, i.e., the position sensors' readings from the actuators and the hologram recordings from the DHM. These measurements are synchronously recorded with a minimum delay to minimize the effect of noise at this nanometric scale. Additionally, the DHM can output reconstructed images, i.e., intensity and phase images, from each recorded hologram. These images are subsequently used in Matlab to estimate the 6-DoF pose of precision positioning systems using the methods explained earlier.

B. Characterization of out-of-plane measurements

Table I specifies the values of different performance metrics for the proposed measurement method for out-of-plane components. The table also encapsulates the values of perfor-
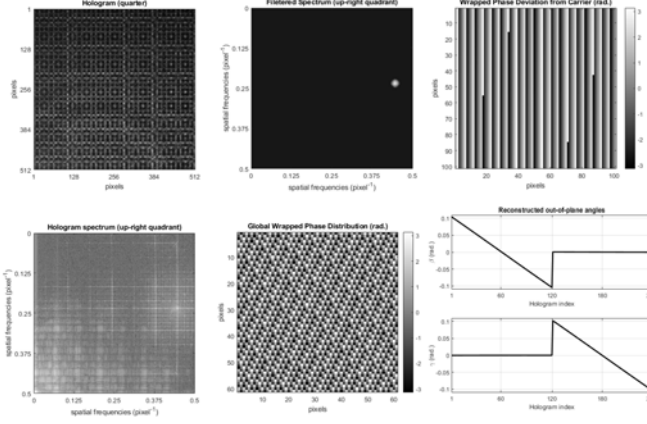
Figure 5. Measurement range of out-of-plane angles. *(Top-left)* Small zone of the recorded hologram. *(Bottom-left)* Upper-right quadrant of the Fourier spectrum of the hologram. *(Top-center)* Upper-right quadrant of the Fourier spectrum of the hologram after narrow band-pass filtering around the current frequency carrier lobe. *(Bottom-center)* Wrapped phase map associated with the current frequency carrier. *(Top-right)* Wrapped phase after subtraction of the frequency carrier when both β and γ angles are equal to zero. *(Bottom-right)* Measured range for β and γ angles, respectively. (cf supplementary video 1).

mance metrics corresponding to the in-plane measurements as characterized previously [18]. In the following sub-sections, the characteristics of the out-of-plane measurement will be detailed.

Measurement resolution: The resolution of a measurement system is the smallest change in the position being measured [42]. Here, the resolution of the three out-of-plane components z, β, and γ of the measurement was confirmed. For this, three experiments were conducted to confirm the measurement resolution using the 3-DoF nanopositioning stage as a reference system. Square waves with descending amplitudes were applied on each of the stage axes. Subsequently, the position of the piezo stage was sampled by both the stage position sensors and the proposed measurement method with approximately 40 samples for each square wave. Fig. 4(a-c) show the measurement results of the z, β, and γ components, respectively. The black lines, red lines, blue-solid lines, and blue-dashed lines show the reference position measurements from the position sensors of the piezo stage, position measurements using the proposed method, mean measured position using the proposed method, and standard deviation using the proposed method, respectively. In Fig. 4(a), the z-axis of the piezo stage was displaced using square waves with amplitudes of 10, 5, and 1 nm, respectively. As evident in Figs. 4(b) and 4(c), the β-angle and γ-angle of the piezo stage were displaced using square waves with amplitudes of 2, 1, 0.5, and 0.1 μrad, respectively. The figures show that the resolution of the proposed method can reach down to 1 nm on the z-axis, 0.1 μrad on the β-angle, and 0.1 μrad on the γ-angle, where the high and low signals can be distinguished.

The noise in the measurements is primarily ascribable to disturbances such as mechanical vibrations and air motion.

Measurement linearity: Linearity represents the closeness of the agreement between the results of measurements of a continuous variable, obtained by a measuring system for indications or values, and the corresponding values realized by the reference standard [42]. In this study, the measurement linearity of the three out-of-plane components was confirmed. For this, the full range of the piezo stage for z, β, and γ was scanned with increasing steps. The z-axis full range of 200 μm, β-angle full range of 2 mrad (-1 to +1 mrad), and γ-angle full range of 2 mrad (-1 to +1 mrad) were scanned with incremental steps of 100 nm, 100 μrad, and 100 μrad, respectively. The position of the piezo stage was sampled using stage position sensors and the proposed measurement method with approximately 20 samples for each step.

Fig. 4(d-f) show the measurement results of the z, β, and γ components, respectively. Here, the horizontal axis of the figures represents the reference position measurements from the piezo stage sensors. The red crosses show the position measurements using the proposed method by taking the mean value of each step of the full-range scan. The black lines, magenta-dashed lines, and blue lines represent the least square linear fit of the measured points (red crosses), standard deviation of the linear fit, and linearity error (the difference between the measured points and the linear fit). Linearity was calculated as the percentage of the maximum linearity error over the full displacement range. For the z-axis, linearity was 0.03%, with an absolute linearity error of less than 62 nm. For the β-angle, linearity was 1%, with an absolute linearity error of less than 20 μrad. For the γ-angle, linearity was 0.51%, with an absolute linearity error of less than 11 μrad.

Measurement range: The displacement and angular ranges mentioned above reflect the allowed motion ranges of the piezo stage. For the z-axis, the stage displacement range of 200 μm corresponds to the measurement range allowed by the DHM. However, for β-angle and γ-angle, the measurement range is larger than the allowed angular displacement of the piezo stage. Thus, the full measurement range of the out-of-plane angles was confirmed here using the precision hexapod, which can reach higher angular displacements. This was performed by scanning an angular displacement range of 0.21 rad (-0.105 to +0.105 rad) on both angles with steps of 0.0017 rad. One sample was recorded at each step using the position sensors of the hexapod and the proposed method. Fig. 12 shows the full-range scan results for both out-of-plane angles, where the total measurement range of the proposed method for both angles can be confirmed at 0.21 rad. In addition, no noticeable difference in the measurement performance at the range limits of the proposed method was observed. The displacement of the Fourier frequency spectrum used to infer the angular displacement is presented in the supplementary video 1. This angular range limit is intrinsic to the DHM due to the limitations in the depth-of-focus and the numerical aperture of the objective lens.

In comparison with the 200 μm z-range, the 110 mm x and y ranges are very large. In-plane and out-of-plane measurement ranges are independent of each other, leading to this high disproportion ratio that may be limiting in some applications. However, in the case of 2D stick-slip actuators for instance, our method would provide a unique means to characterize the 6-DoF behavior of the robot over its full lateral range. In such a particular application, the 0.2 mm z-range would be sufficient

Table I
PERFORMANCE METRICS OF THE PROPOSED 6-DoF MEASUREMENT METHOD.

	In-plane components			Out-of-plane components		
	x	y	α	z	β	γ
Resolution	0.96 nm	0.77 nm	4 µrad	1 nm	0.1 µrad	0.1 µrad
Linearity	0.4%	0.4%	0.00024%	0.03%	1%	0.51%
Repeatability	n/a	n/a	n/a	0.12 nm	0.03 µrad	0.04 µrad
Range	110 mm	110 mm	2π rad	0.2 mm	0.21 rad	0.21 rad
Ambiguity	n/a	n/a	2π rad	337.5 nm	n/a	n/a

Table II
COMPARISON OF THE RESOLUTIONS AND RANGES OF STATE-OF-THE-ART 6-DoF MEASUREMENT SYSTEMS.

		x	y	z	α	β	γ
Lee et al. [13]	Resolution	0.4 nm	20 nm	20 nm	0.15 µrad	0.15 µrad	0.15 µrad
	Range	40 mm	0.8 mm	0.8 mm	2 mrad	2 mrad	2 mrad
Hsieh et al. [15]	Resolution	2 nm	2 nm	2 nm	0.05 µrad	0.05 µrad	0.05 µrad
	Range	50 mm	50 mm	1.2 mm	1 mrad	0.8 mrad	0.8 mrad
Li et al. [16]	Resolution	<1 nm	<1 nm	<1 nm	0.5 µrad	0.5 µrad	0.5 µrad
	Range	15 µm	15 µm	15 µm	0.3 mrad	0.3 mrad	0.3 mrad
Jäger [41]	Resolution	0.02 nm	0.02 nm	0.02 nm	0.01 µrad	0.01 µrad	0.01 µrad
	Range	200 mm	200 mm	25 mm	0.86 mrad	0.86 mrad	0.86 mrad
This work	Resolution	0.96 nm	0.77 nm	1 nm	4 µrad	0.1 µrad	0.1 µrad
	Range	110 mm	110 mm	0.2 mm	2π rad	0.21 rad	0.21 rad

to quantify the out-of-plane robot deviations.

Measurement repeatability: Measurement repeatability is defined as the measurement precision under a set of repeatability conditions of measurement [42]. Here, the measurement repeatability of the three out-of-plane components was confirmed. For this, repeated square waves having equal amplitudes and duty cycles were applied on each axis of the piezo stage. The total number of steps for each axis was 2500 steps. Each step was sampled by the stage position sensors and the proposed measurement method with approximately 20 samples. The amplitudes of the applied square waves were 25 nm, 50 µrad, and 50 µrad for z, β, and γ, respectively. To confirm the repeatability, the measured distances by the proposed method were computed for each step of the square waves using the mean of the samples of each high and low signal. Subsequently, the repeatability error was confirmed through normalization using the mean value of the measured distances. Fig. 4(g-i) represent the histograms of the repeatability error for z, β, and γ, respectively. From the results, a repeatability of 0.12 nm, 0.03 µrad, and 0.038 µrad was confirmed for z, β, and γ, respectively.

Table II compares the resolution and range of the proposed system to other 6-DoF measurement systems. In terms of resolution, our system provides comparable performance to other works for both translational and rotational components. Only the nanomeasuring machine in [41] offers better resolution thanks to the use of top interferometers based on 632.8 nm

HeNe lasers. In terms of range, our system provides considerably superior ranges, specifically in angle measurements α, β, and γ.

C. Application to 6-DoF robotics

Many factors affect the ability of a robot to position accurately at the micro and nano scales: assembly errors, stage travel errors (straightness, flatness, runout, pitch, roll, yaw), backlash errors, and encoder errors. For instance, a perpendicularity error of 0.1° between the x and y stages of a 2D positioning system would lead to a 20 µm positioning error over a motion of 20 mm [43]. Consequently, various works have investigated motion errors in positioning systems, where translation error values down to several nanometers and rotation error values down to several microradians could be confirmed [44]. In this section, The proposed 6-DoF measurement method was applied to a 6-DoF precision hexapod to demonstrate its performance in a real case. The primary purpose of the following experiments was to demonstrate the ability of the proposed method to track the actual trajectory of precision positioning systems in space along two trajectories; a line and a circle. These trajectories are typically applied to evaluate the performance of positioning systems by measuring their travel errors, which were summarized in Table III.

Fig. 6 shows the experimental results of the 6-DoF measurement of the line trajectory. Fig. 6(a) illustrates the trajectory, showing the motion of the pseudo-periodic pattern fixed on
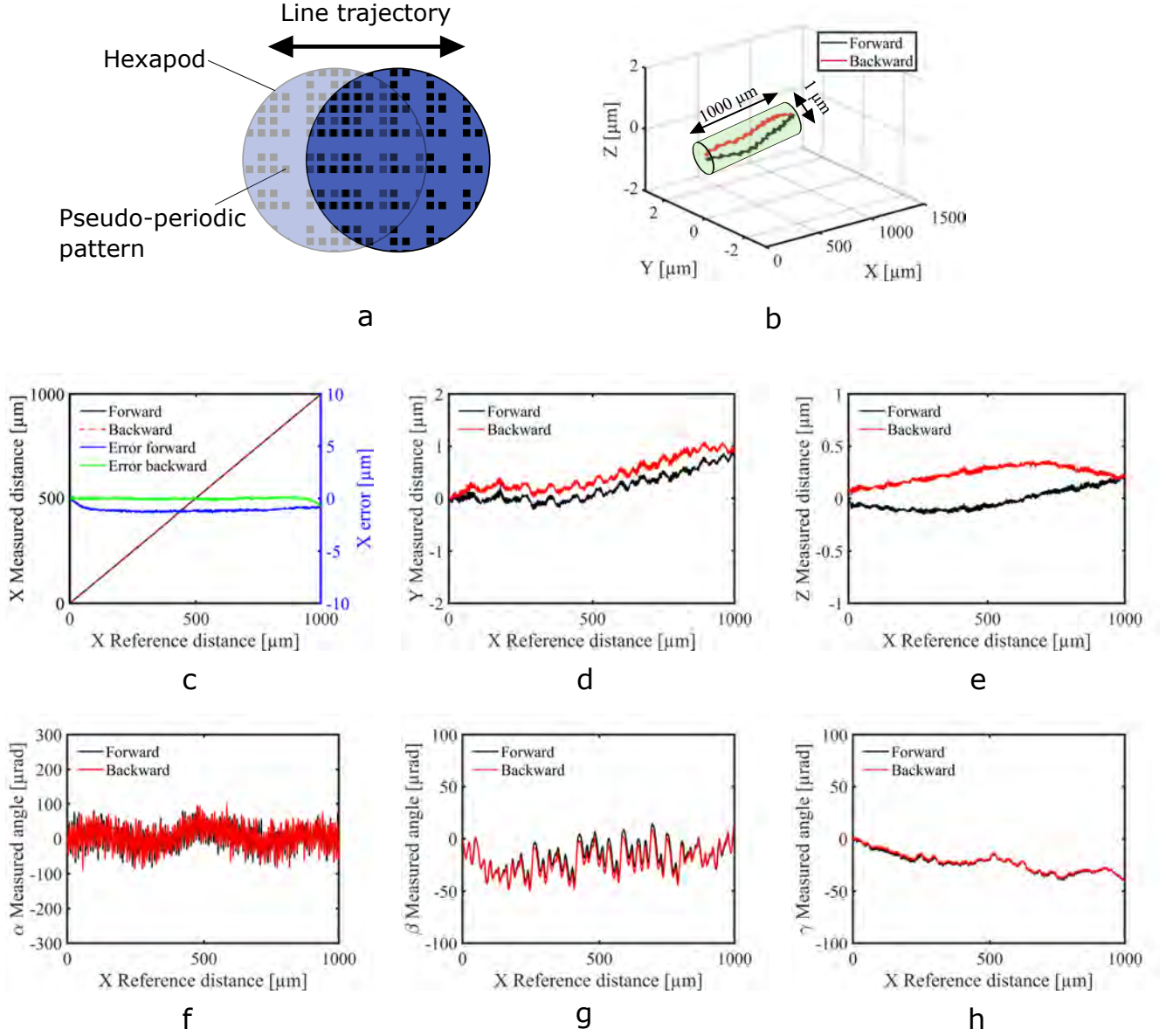
Figure 6. Application to 6-DoF robotics with a line trajectory using a 6-DoF precision hexapod. The trajectory is composed of a forward and a backward line trajectory on the x-axis. (a) Illustration of the line trajectory showing the motion of the pseudo-periodic pattern. (b) The 3D trajectory of the hexapod measured by the proposed method. The black and red lines show the forward and backward motions, respectively. The light-green cylinder encapsulates the displacement errors of the full trajectory. (c) Distance on the x-axis. The black and red-dashed lines represent the forward and backward trajectories, respectively. The right-hand side axis (in blue) shows the error on the x-axis, where the blue line and green line represent the errors for the forward and backward trajectories, respectively. (d-h) Distances and angles on the y, z, α, β, and γ components of the trajectory. The black and red lines represent the forward and backward trajectories, respectively.

the hexapod in a linear trajectory. A forward and backward line trajectory with a length of 1000 μm on the x-axis with steps of 1 μm was applied to the hexapod. At each step, the 6-DoF position of the hexapod was registered using the hexapod position sensors and proposed method. Fig. 6(b) shows the 3D trajectory of the hexapod, and Fig. 6(c-h) show the six components x, y, z, α, β, and γ of the trajectory measured using the proposed method against the x-axis position measured by the hexapod sensors. The black and red lines show the forward and backward trajectories, respectively. Fig. 6(c) also shows the measured error on the x-axis, where the blue line and green

line show the error for the forward and backward trajectories, respectively. The peak-to-peak error was less than 2 μm for the total trajectory. In addition, it can be observed from Fig. 6(b) that the actual trajectory of the hexapod was not purely linear, where erroneous motions on both the y-axis and z-axis can be confirmed. The light-green cylinder in the figure encapsulates the total trajectory and shows that a peak-to-peak error of up to 1 μm on the y-axis and z-axis was generated for an x-axis displacement of 1000 μm. These errors can also be confirmed clearly in Fig. 6(d, e). Using these measurements, straightness (i.e. maximal error on y-axis) and flatness (i.e. maximal error
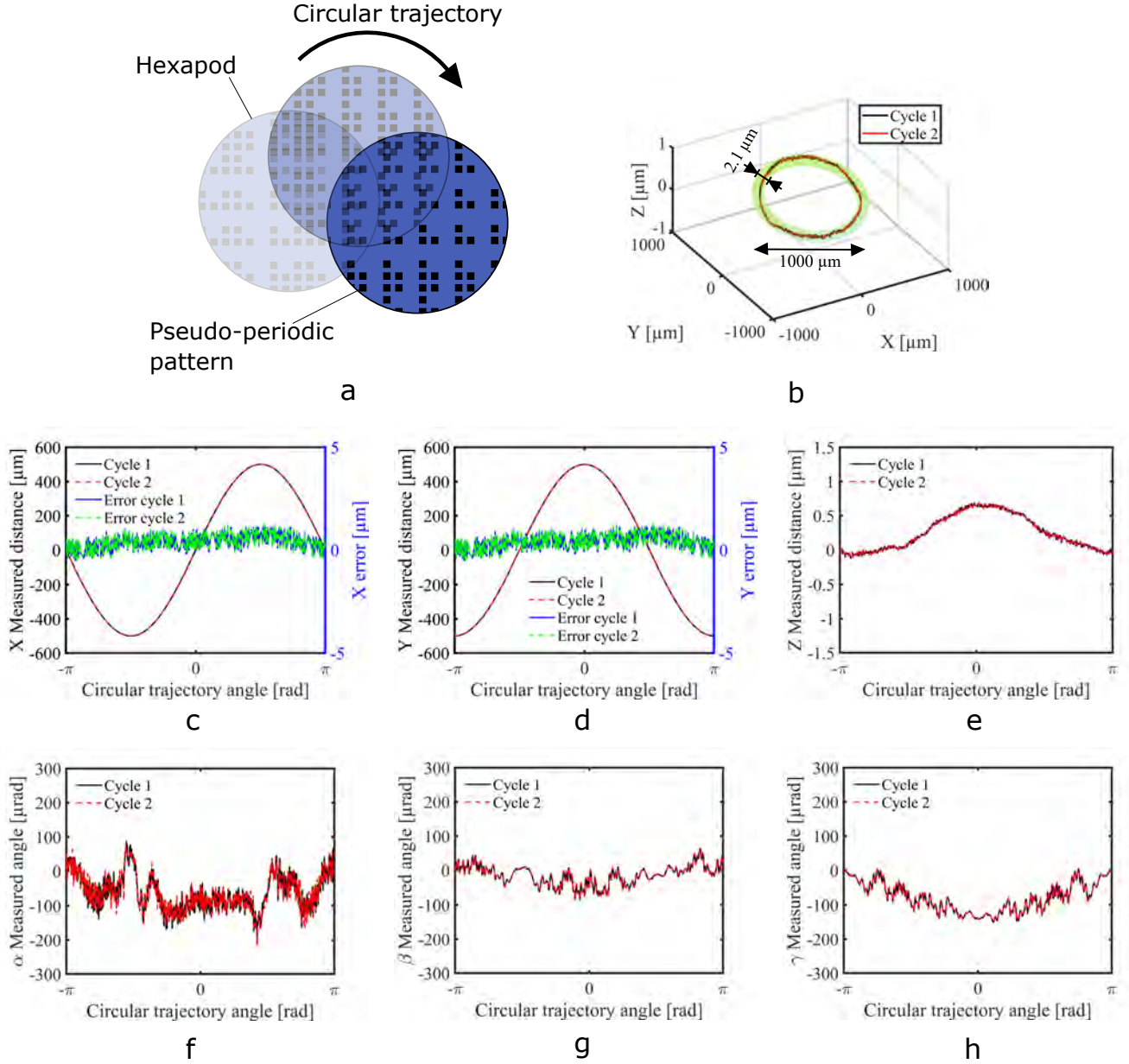
Figure 7. Application to 6-DoF robotics with a circle trajectory using a 6-DoF precision hexapod. The trajectory is composed of two circular cycles applied as two phase-shifted sinusoidal waves to the x-axis and y-axis. (a) An illustration of the circle trajectory showing the motion of the pseudo-periodic pattern. (b) The 3D trajectory of the hexapod measured by the proposed method. The black line and red line show the first and second cycles, respectively. The light-green torus encapsulates the displacement errors of the full trajectory. (c, d) Distances on the x-axis and y-axis. The black and red-dashed lines represent the first and second cycles, respectively. The right-hand side axis (in blue) shows the error on the x-axis and y-axis, where the blue line and green-dashed line represent the errors for the first and second cycles, respectively. (e-h) Distances and angles on the z, α, β, and γ components of the trajectory. The black and red-dashed lines represent the first and second cycles, respectively.

on z-axis) were confirmed to be 1.08 μm and 0.362 μm, respectively. Moreover, angular motion errors were observed on all three angular components of the trajectory, as shown in Fig. 6(f-h). Using these measurements, yaw maximal deviation (i.e. maximal error on α-angle), pitch maximal deviation (i.e. maximal error on β-angle), and roll maximal deviation (i.e. maximal error on γ-angle) were confirmed to be 100 μrad, 49.5 μrad, and 39.4 μrad, respectively.

Fig. 7 shows the experimental results of the 6-DoF measurement of the circle trajectory. An illustration of the trajectory is represented in Fig. 7(a), showing the motion of the pseudo-periodic pattern fixed on the hexapod in a circular trajectory. Two sinusoidal trajectories with peak-to-peak amplitudes of 1000 μm and frequencies of 0.0014 Hz were applied on both the x-axis and y-axis of the hexapod, where the y-axis sinusoidal trajectory had a $\pi/2$ phase shift to generate a planar circular trajectory. The circle trajectory was sampled at each 8.7 mrad, i.e., 0.5 degrees, where the position of the hexapod was measured using the hexapod sensors and the proposed method. Fig. 7(b) shows the 3D trajectory of the hexapod, and
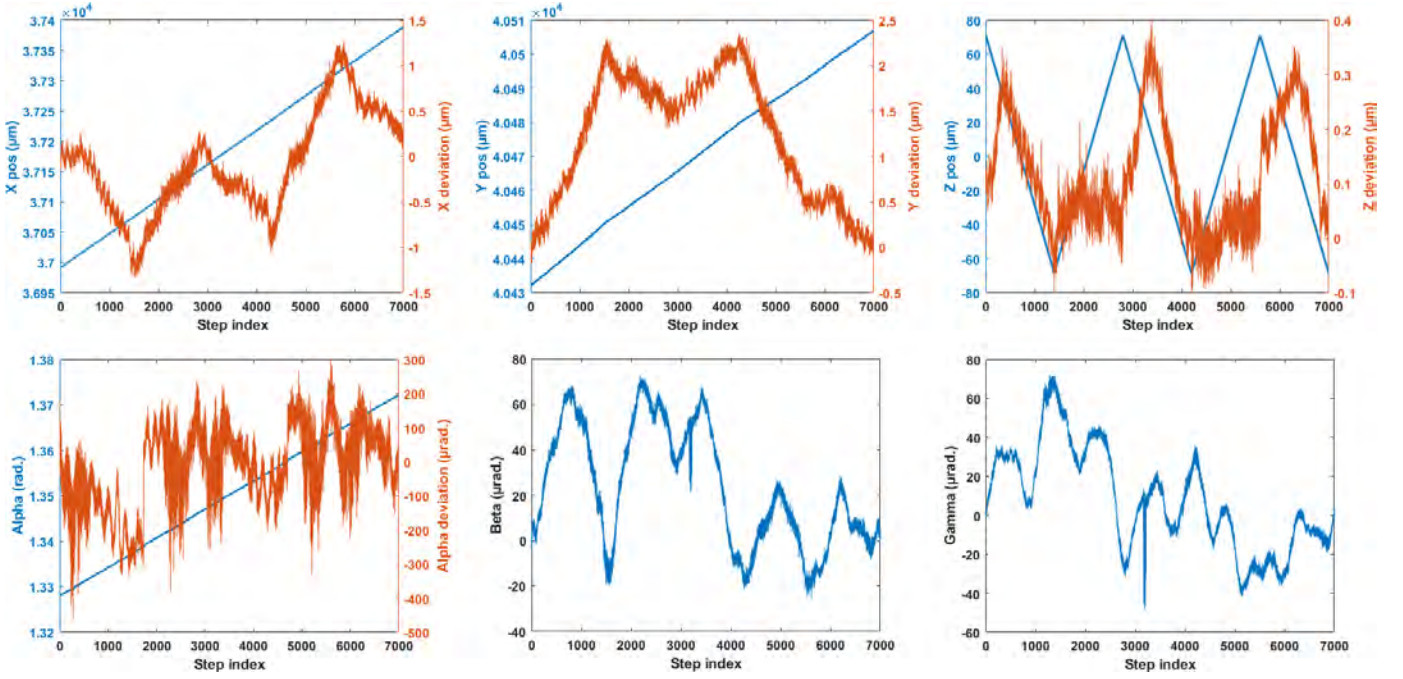
Figure 8. 6-DoF measurement results for a z-triangular trajectory of the precision hexapod combined with a linear α rotation. 140 μm z-excursion by steps of 0.1 μm and 45 mrad α-excursion by steps of 6.4 μrad.

Fig. 7(c-h) show the six components x, y, z, α, β, and γ of the trajectory measured using the proposed method against the angle of the circle trajectory measured by the hexapod sensors. The black and red-dashed lines show the first and second cycles of the circle trajectories, respectively. Fig. 7(c, d) also show the measured error on the x-axis and y-axis, where the blue line and green line show the error for the first cycle and second cycle, respectively. The peak-to-peak error on the x-axis was less than 1.8 μm, and the peak-to-peak error on the y-axis was less than 2.1 μm for both cycles. Moreover, Fig. 7(b) demonstrates that the actual trajectory of the hexapod was not purely planar, where erroneous motion on the z-axis can be observed. The light-green torus in the figure encapsulates the total trajectory and shows that a peak-to-peak error of less than 0.9 μm on the z-axis was generated. This error can also be confirmed clearly in Fig. 7(e). Using these measurements, radial runout error (i.e. maximal error in radial direction) and axial runout error (i.e. maximal error on z-axis) were confirmed to be 0.999 μm and 0.7 μm, respectively. Similar to the case of a line trajectory, angular motion errors were observed on all three angular components of the trajectory, as shown in Fig. 7(f-h). Using these measurements, yaw maximal deviation, pitch maximal deviation, and roll maximal deviation were confirmed to be 217 μrad, 86.1 μrad, and 150.9 μrad, respectively.

A supplementary precision hexapod characterization was performed by applying a z-triangular input command combined with a linear in-plane α-rotation. 6-DoF results are presented in Fig. 8. We observe that the measured deviation from the expected hexapod trajectory is related to the triangular input command with some degree of coupling and delay between the different DoFs. The applied in-plane rotation

Table III
PERFORMANCE METRICS OF THE PRECISION HEXAPOD.

	Linear motion	Circular motion
Travel length / diameter	1 mm	1 mm
Straightness / radial runout	1.08 μm	0.999 μm
Flatness / axial runout	0.362 μm	0.7 μm
Yaw maximal deviation	100 μrad	217 μrad
Pitch maximal deviation	49.5 μrad	86.1 μrad
Roll maximal deviation	39.4 μrad	150.9 μrad

induces noticeable x and y displacements due to the non-alignment between the rotation axes of the hexapod and the DHM. Such results demonstrate the proposed method capabilities to characterize accurately robot responses to various trajectories.

IV. DISCUSSION

The relatively low speed of the applied trajectory was chosen to allow the hexapod to stabilize at its target position with the best possible accuracy. The displacement speed is limited in two ways; i.e. the DHM frame rate (150fps) and the maximal z-step between consecutive holograms (25 μm/s in single wavelength). Indeed, due to the entire number of periods ambiguity and the use of reflective DHM, two consecutive samples should not be spaced by more than $\lambda/4$ on the z-axis. Considering the maximum frame rate of the DHM of 150 fps, the maximum vertical motion speed should be less than 25 μm/s to achieve a correct phase unwrapping. However,

this speed limit can be extended further by using a second wavelength to enlarge the unambiguity range as currently used in interferometry. The equivalent wavelength is given by: $\Lambda = \lambda_1.\lambda_2/(\lambda_1 - \lambda_2)$, where λ_1, λ_2 are the laser wavelengths used, and Λ the resulting equivalent wavelength [35]. In practice, the two wavelengths are angularly multiplexed in the hologram and the DHM system still works as single shot recording at the same frame rate.

The accuracy of the measurements relies on the calibration of the measurement system. As the developed method relies on the combination of interferometry and phase-based motion estimation, the accuracy is based on the wavelength of the laser for out-of-plane measurements and the micro-structured pattern fabrication for in-plane measurements. The light source is a super luminescent laser diode filtered by a 1 nm bandwidth interference filter, thus ensuring high wavelength stability of 675 nm. The pattern is made of quartz and has been realized using a high-resolution maskless aligner (Heidelberg MLA150). The in-plane measurement uses the phase of the pattern to estimate its pose. This process depends only on the physical period of the pattern. The size of the dots does not influence the measurement. Owing to the high selective bandwidth filtering, the method is also robust to dust and other local artifacts.

V. CONCLUSION

In this article, we have proposed a method to measure the six DoFs of an object moving in space with nanometric resolutions over millimetric ranges with a single device and a single shot. The measurement principle is based on off-axis digital holography and involves interferometry and phase-based motion estimation, applied simultaneously to the hologram of a microstructured pattern.

The performance metrics, namely, resolution, linearity, range, and repeatability, have been experimentally evaluated. The resolution of the method can reach down to 1 nm for the three translations, 0.1 µrad for tip and tilt angles, and 4 µrad for z-axis rotation. The range of measurement reaches 110 mm for x and y displacements, 0.2 mm for z, 0.21 rad for tip and tilt angles and 2π rad for z-axis rotations.

To demonstrate the potential of the method for 3D metrology applications, the technique has been applied to the characterization of a precision hexapod. It is shown that the robot only deviates from 1 µm over a 1 mm long straight path, while its orientation errors remain below 200 µrad.

REFERENCES

[1] M. Kirkpatrick, D. Sander, F. El Kalach, and R. Harik, "Motion capture based calibration for industrial robots," Manufacturing Letters, vol. 35, pp. 926–932, 2023.

[2] M. Menolotto, D.-S. Komaris, S. Tedesco, B. O'Flynn, and M. Walsh, "Motion capture technology in industrial applications: A systematic review," Sensors, vol. 20, no. 19, p. 5687, 2020.

[3] M. Nagy, H. Naik, F. Kano, N. V. Carlson, J. C. Koblitz, M. Wikelski, and I. D. Couzin, "Smart-barn: Scalable multimodal arena for real-time tracking behavior of animals in large numbers," Science Advances, vol. 9, no. 35, p. eadf8068, 2023.

[4] A. Sorriento, M. B. Porfido, S. Mazzoleni, G. Calvosa, M. Tenucci, G. Ciuti, and P. Dario, "Optical and electromagnetic tracking systems for biomedical applications: A critical review on potentialities and limitations," IEEE Reviews in Biomedical Engineering, vol. 13, pp. 212–232, 2019.

[5] S. J. Keating, J. C. Leland, L. Cai, and N. Oxman, "Toward site-specific and self-sufficient robotic fabrication on architectural scales," Science Robotics, vol. 2, no. 5, p. eaam8986, 2017.

[6] R. K. Sahu et al., "A review on application of laser tracker in precision positioning metrology of particle accelerators," Precision Engineering, vol. 71, pp. 232–249, 2021.

[7] A. Nubiola, M. Slamani, A. Joubair, and I. A. Bonev, "Comparison of two calibration methods for a small industrial robot based on an optical cmm and a laser tracker," Robotica, vol. 32, no. 3, pp. 447–466, 2014.

[8] X. Liu, K. Peng, Z. Chen, H. Pu, and Z. Yu, "A new capacitive displacement sensor with nanometer accuracy and long range," IEEE Sensors Journal, vol. 16, no. 8, pp. 2306–2316, 2016.

[9] S. Chen, J. Luo, X. Wang, Q. Li, L. Zhou, C. Liu, and C. Feng, "Fabrication and piezoresistive/piezoelectric sensing characteristics of carbon nanotube/pva/nano-zno flexible composite," Scientific Reports, vol. 10, no. 1, p. 8895, 2020.

[10] W. Li, Y. Ye, K. Zhang, and Z. Feng, "A thickness measurement system for metal films based on eddy-current method with phase detection," IEEE Transactions on Industrial Electronics, vol. 64, no. 5, pp. 3940–3949, 2017.

[11] G. H. Yuan and N. I. Zheludev, "Detecting nanometric displacements with optical ruler metrology," Science, vol. 364, no. 6442, pp. 771–775, 2019.

[12] A. J. Fleming, "A review of nanometer resolution position sensors: Operation and performance," Sensors and Actuators A: Physical, vol. 190, pp. 106–126, 2013.

[13] C. Lee, G. H. Kim, and S.-K. Lee, "Design and construction of a single unit multi-function optical encoder for a six-degree-of-freedom motion error measurement in an ultraprecision linear stage," Measurement Science and Technology, vol. 22, no. 10, p. 105901, 2011.

[14] I. Ortlepp, "High-precision nanopositioning and nanomeasuring machines for alternative nanofabrication," in Novel Patterning Technologies 2024, vol. 12956. SPIE, 2024, pp. 90–106.

[15] H.-L. Hsieh and S.-W. Pan, "Development of a grating-based interferometer for six-degree-of-freedom displacement and angle measurements," Optics express, vol. 23, no. 3, pp. 2451–2465, 2015.

[16] X. Li, Y. Shimizu, T. Ito, Y. Cai, S. Ito, and W. Gao, "Measurement of six-degree-of-freedom planar motions by using a multiprobe surface encoder," Optical Engineering, vol. 53, no. 12, pp. 122 405–122 405, 2014.

[17] S. Yao, H. Li, S. Pang, B. Zhu, X. Zhang, and S. Fatikow, "A review of computer microvision-based precision motion measurement: Principles, characteristics, and applications," IEEE Transactions on Instrumentation and Measurement, vol. 70, pp. 1–28, 2021.

[18] A. N. André, P. Sandoz, B. Mauzé, M. Jacquot, and G. J. Laurent, "Sensing one nanometer over ten centimeters: A microencoded target for visual in-plane position measurement," IEEE/ASME Transactions on Mechatronics, vol. 25, no. 3, pp. 1193–1201, 2020.

[19] O. Acher, T.-L. Nguyên, A. Podzorov, M. Leroy, P.-A. Carles, and S. Legendre, "An efficient solution for correlative microscopy and co-localized observations based on multiscale multimodal machine-readable nanogps tags," Measurement Science and Technology, vol. 32, no. 4, p. 045402, 2021.

[20] A. N. André, O. Lehmann, J. Govilas, G. J. Laurent, H. Saadana, P. Sandoz, V. Gauthier, A. Lefèvre, A. Bolopion, J. Agnus et al., "Automating robotic micro-assembly of fluidic chips and single fiber compression tests based-on xyθ visual measurement with high-precision fiducial markers," IEEE Transactions on Automation Science and Engineering, 2022.

[21] L. Liu and H. Xie, "3-d confocal laser scanning microscopy based on a full-mems scanning system," IEEE Photonics Technology Letters, vol. 25, no. 15, pp. 1478–1480, 2013.

[22] Y. Tan, W. Wang, C. Xu, and S. Zhang, "Laser confocal feedback tomography and nano-step height measurement," Scientific Reports, vol. 3, no. 1, p. 2971, 2013.

[23] P. Sandoz, "Nanometric position and displacement measurement of the six degrees of freedom by means of a patterned surface element," Applied Optics, vol. 44, no. 8, pp. 1449–1453, 2005.

[24] Y. Morita, T. Matsuo, S. Maeda, M. Oishi, and M. Oshima, "Three-dimensional displacement measurement of self-oscillating gel using digital holographic microscopy," Applied Optics, vol. 57, no. 36, pp. 10 541–10 547, 2018.

[25] M. Panahi, R. Jamali, V. F. Rad, M. Khorasani, A. Darudi, and A.-R. Moradi, "3d monitoring of the surface slippage effect on micro-particle sedimentation by digital holographic microscopy," Scientific Reports, vol. 11, no. 1, p. 12916, 2021.

[26] Y. Song, C. Gui, Z. Huo, S. R. Lee, and S. Liu, "Mechanical system and dynamic control in photolithography for nanoscale fabrication: A critical review," International Journal of Mechanical System Dynamics, vol. 1, no. 1, pp. 35–51, 2021.

[27] M. Leveziel, W. Haouas, G. J. Laurent, M. Gauthier, and R. Dahmouche, "Migribot: A miniature parallel robot with integrated gripping for high-throughput micromanipulation," Science Robotics, vol. 7, no. 69, p. eabn4292, 2022.

[28] J. Claverley and R. Leach, "A review of the existing performance verification infrastructure for micro-cmms," Precision engineering, vol. 39, pp. 1–15, 2015.

[29] K. W. Lyons and M. T. Postek, "Metrology at the nanoscale: what are the grand challenges?" in Instrumentation, Metrology, and Standards for Nanomanufacturing II, vol. 7042. SPIE, 2008, pp. 9–21.

[30] R. Leach, Fundamental principles of engineering nanometrology. Elsevier, 2014.

[31] G. Adam, M. Boudaoud, V. Reynaud, J. Agnus, D. J. Cappelleri, and C. Clévy, "An overview of microrobotic systems for microforce sensing," Annual Review of Control, Robotics, and Autonomous Systems, vol. 7, 2024.

[32] Z. Chen, D. Zhou, H. Liao, and X. Zhang, "Precision alignment of optical fibers based on telecentric stereo microvision," IEEE/ASME Transactions on Mechatronics, vol. 21, no. 4, pp. 1924–1934, 2016.

[33] A. N. André, P. Sandoz, B. Mauzé, M. Jacquot, and G. J. Laurent, "Robust phase-based decoding for absolute (x, y, θ) positioning by vision," IEEE Transactions on Instrumentation and Measurement, vol. 70, pp. 1–12, 2020.

[34] A. N. André, P. Sandoz, M. Jacquot, and G. J. Laurent, "Pose measurement at small scale by spectral analysis of periodic patterns," International Journal of Computer Vision, vol. 130, no. 6, pp. 1566–1582, 2022.

[35] Y.-Y. Cheng and J. C. Wyant, "Two-wavelength phase shifting interferometry," Applied optics, vol. 23, no. 24, pp. 4539–4543, 1984.

[36] T. Colomb, N. Pavillon, J. Kühn, E. Cuche, C. Depeursinge, and Y. Emery, "Extended depth-of-focus by digital holographic microscopy," Optics letters, vol. 35, no. 11, pp. 1840–1842, 2010.

[37] M. Asmad Vergara, M. Jacquot, G. J. Laurent, and P. Sandoz, "Digital holography as computer vision position sensor with an extended range of working distances," Sensors, vol. 18, no. 7, p. 2005, 2018.

[38] U. Schnars, C. Falldorf, J. Watson, W. Jüptner, U. Schnars, C. Falldorf, J. Watson, and W. Jüptner, Digital holography. Springer, 2015.

[39] S. De Nicola, A. Finizio, G. Pierattini, P. Ferraro, and D. Alfieri, "Angular spectrum method with correction of anamorphism for numerical reconstruction of digital holograms on tilted planes," Optics Express, vol. 13, no. 24, pp. 9935–9940, 2005.

[40] P. Langehanenberg, G. von Bally, and B. Kemper, "Autofocusing in digital holographic microscopy," 3D Research, vol. 2, no. 1, pp. 1–11, 2011.

[41] G. Jäger, E. Manske, T. Hausotte, A. Müller, and F. Balzer, "Nanopositioning and nanomeasuring machine npmm-200—a new powerful tool for large-range micro-and nanotechnology," Surface Topography: Metrology and Properties, vol. 4, no. 3, p. 034004, 2016.

[42] JCGM 200:2012, The International Vocabulary of Metrology – Basic and General Concepts and Associated Terms (VIM). IPM, IEC, IFCC, ILAC, ISO, IUPAC, IUPAP and OIML, 2012.

[43] N. Tan, C. Clévy, G. J. Laurent, P. Sandoz, and N. Chaillet, "Accuracy quantification and improvement of serial micropositioning robots for in-plane motions," IEEE Transactions on robotics, vol. 31, no. 6, pp. 1497–1507, 2015.

[44] Z. Geng, Z. Tong, and X. Jiang, "Review of geometric error measurement and compensation techniques of ultra-precision machine tools," Light: Advanced Manufacturing, vol. 2, no. 2, pp. 211–227, 2021.

SUPPLEMENTARY MATERIALS

Supplementary Video 1: AngleMeasure.avi

This video presents the principle of out-of-plane angle measurement. The spectral lobe associated with the fringe carrier is progressively shifted as the pattern observed is titled following β and γ. The full range of 0.11 rad explored here is limited by the numerical aperture of the $10\times$ microscope lens used.

Supplementary Video 2: Z-ScanPrinciple.avi

This video illustrates the measurement principle of the pattern motion following the z direction. As the object is moved upward, interference fringes are shifted to the right. The resulting phase map is also shifted and, after phase unwrapping, the continuous motion of the pattern along z direction is retrieved.

Supplementary Video 3: PatternReconstructionPrinciple.avi

This video presents the numerical reconstruction of the pattern from the hologram recorded at an out-of-focus distance. The first diffraction order is filtered from the hologram spectrum. Then a propagator is applied under the form of a phase term corresponding to the desired focusing distance for every spectral component. Finally, an inverse Fourier transform provides the reconstructed object in both phase and intensity. The latter images are suited for further in-plane position calculations.
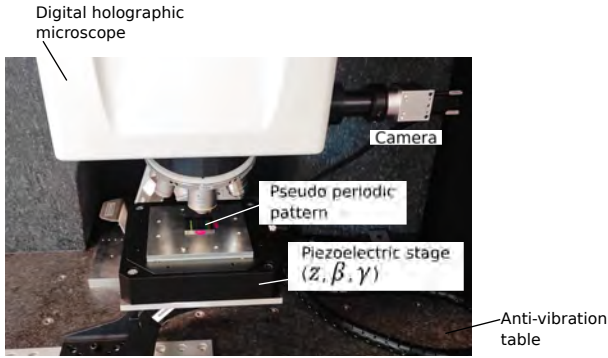

Figure 9. Experimental setup of the characterization system showing the DHM and the piezoelectric stage.
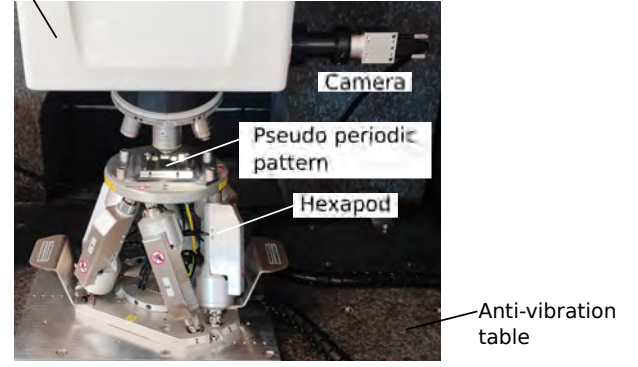

Figure 10. Experimental setup of the 6-DoF trajectory measurement system showing the DHM and the hexapod.
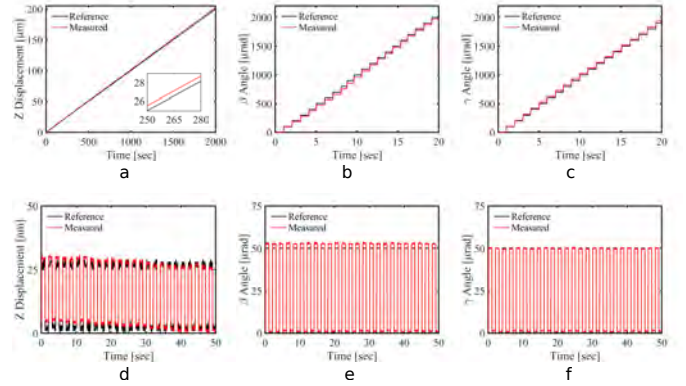

Figure 11. Characterization of out-of-plane measurement. (a-c) Full range scan of the piezoelectric stage for each out-of-plane axis, z, $\boldsymbol{\beta}$, and $\boldsymbol{\gamma}$, respectively. (d-f) Repeatability test using square wave motion for each out-of-plane axis, z, $\boldsymbol{\beta}$, and $\boldsymbol{\gamma}$, respectively.
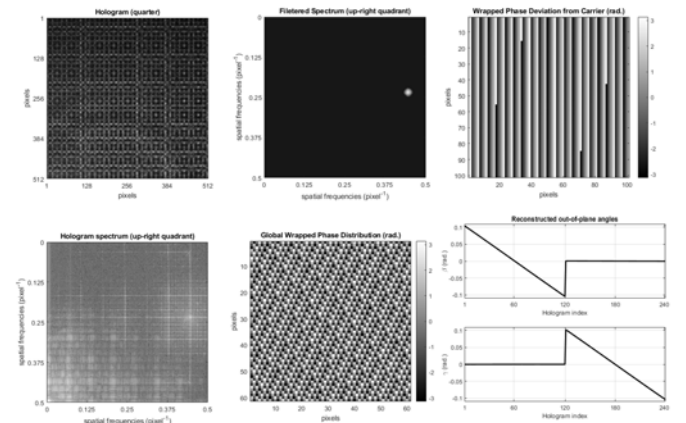

Figure 12. Measurement range of out-of-plane angles. *(Top-left)* Small zone of the recorded hologram. *(Bottom-left)* Upper-right quadrant of the Fourier spectrum of the hologram. *(Top-center)* Upper-right quadrant of the Fourier spectrum of the hologram after narrow band-pass filtering around the current frequency carrier lobe. *(Bottom-center)* Wrapped phase map associated with the current frequency carrier. *(Top-right)* Wrapped phase after subtraction of the frequency carrier when both β and γ angles are equal to zero. *(Bottom-right)* Measured range for β and γ angles, respectively. (cf supplementary video 1).